Creating dual-mode luminescence in piezoelectric calcium niobates through lanthanide-doped for anti-counterfeiting and temperature sensing

W. Yan, Z. Su, R. Ye, L. Chen, Z. Lu, G. Bai, S. Xu

Creating dual-mode luminescence in piezoelectric calcium niobates through lanthanide-doped for anti-counterfeiting and temperature sensing

Wen Yan[1], Zewen Su[1,2], Renguang Ye[1,3*], Liang Chen[2], Zhanling Lu[4], Gongxun Bai[1*], Shiqing Xu[1*]

[1]*Institute of Optoelectronic Materials and Devices, China Jiliang University, Hangzhou 310018, People's Republic of China*

[2]*College of Optics and Electronic Technology, China Jiliang University, Hangzhou 310018, People's Republic of China*

[3]*University Rennes, CNRS, ISCR (Institut des Sciences Chimiques de Rennes)-UMR 6226, F-35000 Rennes, France*

[4]*College of Materials Science and Engineering, Zhengzhou University, Zhengzhou 450001, Henan, People's Republic of China*

*Corresponding author: yerenguang@cjlu.edu.cn, baigx@cjlu.edu.cn, shiqingxu@cjlu.edu.cn

ABSTRACT

Lanthanide-doped luminescent materials have been widely used in the field of information security and optical sensing, owing to their unique optical properties. However, conventional luminescent materials usually exhibit unicolor and single-peak emission, which leads to a decrease in the application efficiency of anti-counterfeiting and optical temperature sensing. In this work, we have successfully developed a series of novel multi-mode stimulation luminescent materials in the $Ca_2Nb_2O_7$ system via the solid phase reaction. This luminescent material is synthesized by doping dual lanthanide ions to realize adjustable multi-mode luminescence, which simultaneously create luminescent centers and carrier traps in the host lattice. The multi-colored emission can be realized under different excitation wavelengths. Meanwhile, it has a combination of fluorescent phenomenon by upconversion, down-shifting and thermal stimulation. In addition, the fluorescence intensity ratio of lanthanide ions shows significant temperature dependence, and the maximum S_r is 0.0072 K^{-1} at 293 K. Hence, we have fabricated a novel material that can be used for multi-mode anti-counterfeiting and optical temperature sensing.

Keywords: Luminescence; Lanthanide; Multi-color emission; Temperature sensing; Anti-counterfeiting

1. Introduction

As the rapid economic development in 21st century, fake and inferior products have penetrated into various industries, such as food, medicine, clothing, chemical industry and so on. Those products have seriously damaged the global economy even human health, that is why the research of the advanced anti-counterfeiting technology is a pressing project of the moment[1-4]. At present, the anti-counterfeiting technology mainly includes paper printing, humidity sensitive anti-counterfeiting, nuclear magnetic resonance anti-counterfeiting, digital anti-counterfeiting, bar code, quick response (QR), laser holography and so on[5, 6]. But these anti-counterfeiting technologies are easy to be copied and high manufacturing costs limit their wide applications. A kind of excellent anti-counterfeiting material should be characterized by unduplicated in certain time limit, reasonable price and the advantage to protect subject information from being copied[7, 8]. Fortunately, fluorescent anti-counterfeiting technology has its unique photoluminescence characteristics which are able to produce sample with tunable property, low-cost and high stability, consequently it becomes a new favorite of anti-counterfeiting researchers[9-15].

Currently, the piezoelectric materials, mainly including piezoelectric crystal materials (such as $LiNbO_3$[16], $GaPO_4$[17]), bismuth layered piezoelectric ceramic materials (such as $SrBi_2Ta_2O_9$[18] and $Bi_4Ti_3O_{12}$[19]) and $A_nB_nO_{3n+2}$ perovskite layered structures (PLS) (such as $Sr_2Nb_2O_7$[20], $Ca_2Nb_2O_7$[21]), have attracted more and more attentions due to their unique advantages. Among them, the PLS ferroelectric material with the general formula $A_nB_nO_{3n+2}$ has important applications

in the field of photochromic and multi-functional devices because of its high sensitivity and inherent piezoelectric characteristics[22, 23]. On the other hand, lanthanide ions doped luminescent materials have been widely used in the fields of optical anti-counterfeiting and display due to their excellent luminescence performance and stability[24-26]. Therefore, a feasible strategy for preparing multi-color fluorescent materials is to introduce lanthanide ions into the piezoelectric and photochromic matrix, so as to realize multi-function and multi-mode luminescence[27, 28]. It is possible to record more information and can't be copied easily anymore. Traditional single-doped lanthanide phosphors usually exhibit monochromatic and unimodal luminescence, while doping lanthanide ions into the piezoelectric material may generate multi-color emissions and have different responses to external stimuli[29]. However, such modulation is rarely reported based on the multi-mode luminescence.

In this work, $Ca_2Nb_2O_7$ as a kind of lead-free piezoelectric material, is selected as host lattice to accommodate both Pr^{3+} and Er^{3+} dopants. We describe a strategy for creating multi-color materials which have tunable luminescence under different stimuli. The luminescent material can exhibit different emission color from red to orange to green by controlling excitation wavelength. Meanwhile as an efficient upconversion luminescent material, the material also exhibits excellent upconversion luminescence characteristics. Based on the thermally coupling energy levels corresponding to Pr and Er ions, sensitive temperature sensing was successfully realized with the developed materials.

2. Experimental

2.1 Preparation of luminescent materials

$Ca_{2-x-y}Nb_2O_7:Pr_x/Er_y$ (x=0, y=0.01; x=0.01, y=0; x=0.01, y=0.01) were prepared by high temperature solid state reaction method. High purity powders of $CaCO_3$ (Aladdin 99.99%), Nb_2O_5 (Aladdin 99.90%), Pr_2O_3 (Aladdin 99.90%), Er_2O_3 (Aladdin 99.99%) were chose as raw materials. The raw materials were weighed accurately according to the stoichiometric ratio, then mixed in agate mortar. During the raw materials mixing, an appropriate amount of anhydrous ethanol was added to ensure fully mixed. The ground powders were ball-milled for 12 h, and pre-sintered at 900 ℃ for 8h. After natural cooling, the pre-sintered powders were mixed with 5% poly (vinyl alcohol) (PVA) solution, then pressed as disc-shaped pallets. Finally, the prepared samples were obtained after sintered at 1400 ℃ for 4 h.

2.2 Physical Characterization

The X-ray diffractometer (XRD, D2 PHASER, AXS, Bruker, Germany) with Cu-K_α radiation was used to identify the phase purity and crystal structure. The microscopic morphology was analyzed by field emission scanning electron microscopy (FE-SEM, SU8010, Hitachi Ltd., Tokyo, Japan). The diffuse reflectance spectrum (DRS) was recorded with the Lamada 750 S spectrophotometer. The emission spectra were collected by the fluorescence spectrometer (FL3, Jobin Yvon, France) with Xenon lamp and a 980 nm laser as the excitation source. The decay curves were recorded with the pulsed Xenon lamp. The temperature dependent emission spectra were measured with the KAP-02 temperature controller.

3. Results and discussion

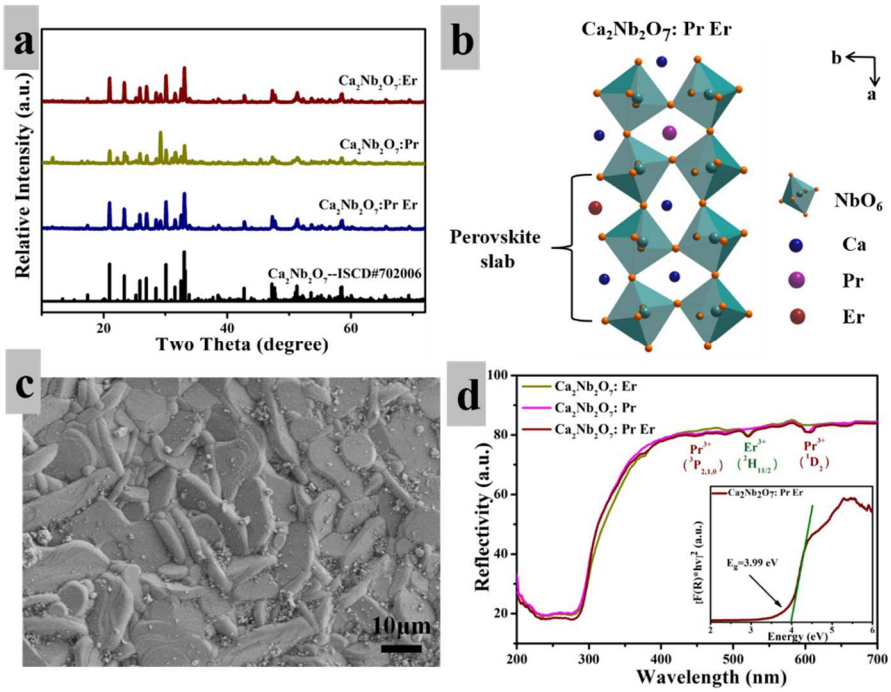

Fig. 1. (a) XRD patterns of the as-prepared $Ca_2Nb_2O_7:Ln^{3+}$ samples. (b) The diagram of the crystal structure in $Ca_2Nb_2O_7:Ln^{3+}$ samples. (c) The SEM image of the $Ca_2Nb_2O_7:Pr^{3+}/Er^{3+}$ disc. (d) Diffuse reflection spectra of the as-synthesized $Ca_2Nb_2O_7:Ln^{3+}$ samples. The inset shows the calculated curve of $(\alpha h\nu)^2$ vs $h\nu$ by using the Kubelka-Munk function.

The XRD patterns of the sintered specimens are shown in Fig**.** 1a. It can be seen that there is no impurity peak in the XRD patterns. The patterns of the doped samples match well with the standard card ISCD#702006 of $Ca_2Nb_2O_7$. Because the ion radii of doped Pr^{3+} and Er^{3+} ions are almost the same as that of Ca^{2+} ions, the crystal structure was not obviously affected by low concentration doping. The structure of perovskite calcium niobate is shown in Fig. 1b. The prepared specimen's system belongs to monoclinic $P2_1$ space group, and the oxygen octahedron is formed by six oxygen octahedron around Nb atoms in calcium niobate crystal[30]. The SEM result of the prepared ceramic sheet sample is shown in the Fig. 1c. The sample shows a dense structure with numerous 1 μm thickness sheets. Fig. 1d indicates the reflection

spectra of phosphor powders doped with praseodymium and erbium prepared by solid-phase reaction. What can be summarized from the figure that is the reflected light of all specimens has a significant decrease around 279 nm, which is due to the valence band to the conduction band in the $Ca_2Nb_2O_7$ matrix lattice absorption[30]. In addition, there are three absorption bands between 300 and 650 nm, which are located at 460, 530, and 610 nm, respectively. These absorption bands can be assigned to the transitions of Pr^{3+}: $^3P_{2,1,0}$, $^1D_2 \rightarrow {}^3H_4$ and Er^{3+}: $^2H_{11/2} \rightarrow {}^4I_{15/2}$[31]. The results indicate that the doped praseodymium ions produced local energy levels within the bandgap of calcium niobate matrix[32]. According to the measured reflection spectra, the band gap width of these specimens was calculated and shown in Fig. 1d. In this work, the experimental value of band gap of $Ca_2Nb_2O_7$ is 3.99 eV which is similar with the previous reports[21].

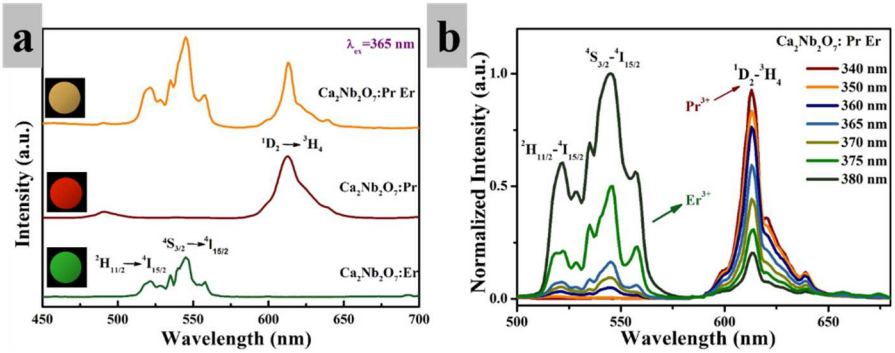

Fig. 2. (a) The emission spectra of the specimens under the excitation of UV light at 365 nm. Insets show optical image under 365 nm excitation. (b) The dependence of the emission spectra on the excitation wavelengths in the range from 340 to 380 nm.

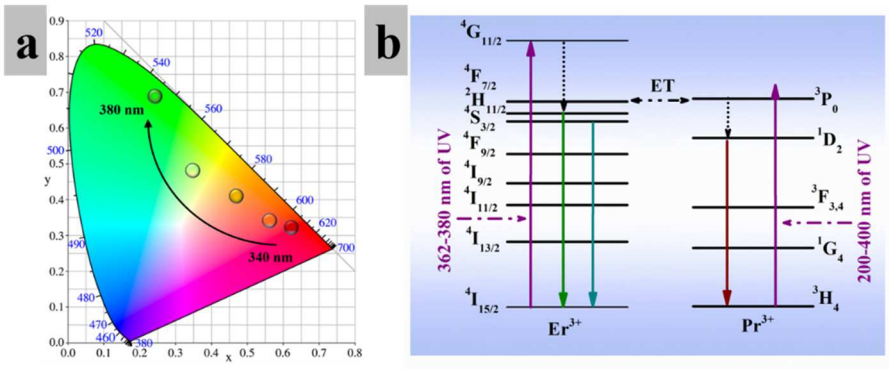

Fig. 3. (a) The CIE chromaticity coordinates of the emission color from the codoped samples with different excitation wavelengths. (b) The proposed energy transfer mechanisms and the luminescence processes of Pr^{3+} and Er^{3+} ions in $Ca_2Nb_2O_7$ hosts.

In Fig. 2a, the emission spectra under the excitation of 365 nm shows multi-colored emissions, including brown, red, and green. These luminescence centers are mainly attributed to the doped lanthanide ions. Specifically, the red emission band centered at 612 nm mainly comes from the energy level transition of Pr^{3+}: $^1D_2 \rightarrow {}^3H_4$, and the green emission bands centered at 545 and 521 nm can be assigned to Er^{3+}: $^2H_{11/2}, {}^4S_{3/2} \rightarrow {}^4I_{15/2}$ transitions, respectively[33]. When Pr^{3+} and Er^{3+} ions are simultaneously introduced into the $Ca_2Nb_2O_7$ matrix and excited by 365 nm light, the spectral combination of red and green emission bands is instantaneously produced from the luminescent ions, leading to brown color[34]. It is interesting to realize the regulation of the luminescence wavelength. The luminescence spectra of the Pr^{3+}/Er^{3+} codoped sample has been recorded under the excitation range from 340 to 380 nm. Fig. 2b shows the tunable colored emission spectra generated from Pr^{3+} and Er^{3+} ions. Among them, different proportions of green/red emission can be observed under excitation in the range from 340 to 380 nm. Therefore, we can obtain continuously adjustable colors according to control different excitation wavelengths. Initially, the

codoped sample was excited by the high-energy light, and Pr^{3+} ions exhibited excellent luminescence performance. As the wavelength increases from 340 to 380 nm, the red emission from Pr^{3+} could not be excited well, while the green emission corresponding to Er^{3+} exhibits great luminescence performance. In addition, it should be noted that the red and green emission peak positions of the codoped specimens have no obvious shift compared to some luminescent nanomaterials. Those results indicate that luminescence center comes from energy level transition of lanthanide ions. In order to observe the color change more intuitively, the display color of the emission spectrum at each excitation wavelength was calculated in the CIE chromaticity coordinates. As indicated in Fig. 3a, the color of the sample is red under high-energy excitation firstly, then the color of the sample gradually shifts from red to orange to green as the excitation wavelength increases later. Therefore, by changing the wavelength of the excitation source, we can achieve a series of continuously color-tunable phosphors. Fig. 3b shows the detailed energy level transition diagram of Pr^{3+} and Er^{3+} ions in the down-shifting luminescence[35-37].

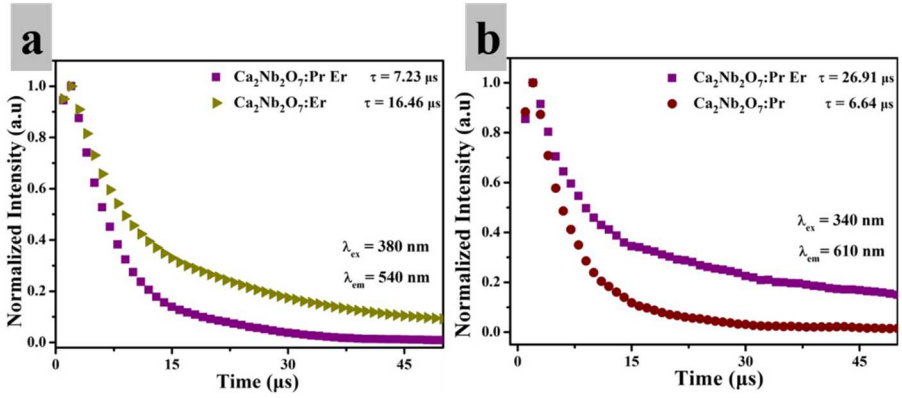

Fig. 4. (a) The decay curves of Er^{3+}-doped and Pr^{3+}/Er^{3+} codoped samples under 380 nm excitation by monitoring the 540 nm emission. (b) The decay curves of Pr^{3+}-doped

and Pr^{3+}/Er^{3+} codoped samples under 340 nm excitation by monitoring the 610 nm emission.

In order to explore the energy transfer mechanism of prepared samples, the decay curves of the prepared samples were measured as shown in Fig. 4. The excitation wavelengths are 380 and 340 nm, corresponding to the emission wavelengths are 540 and 610 nm, respectively. It can be seen from the figure that the lifetime of codoped samples (7.23 μs) is shorter than that of single-doped Er^{3+} (14.46 μs) under 380 nm excitation. It is deduced that the energy transfer from Er^{3+} ions to Pr^{3+} ions leads to shorten lifetime in codoped samples under 380 nm excitation. Conversely the lifetime of codoped samples (26.91 μs) is longer than that of single-doped Pr^{3+} (6.64 μs) is obtained under 340 nm excitation. The fluorescence lifetime of the sample increases due to the energy transfer from Er^{3+} ions to Pr^{3+} ions under 340 nm excitation.

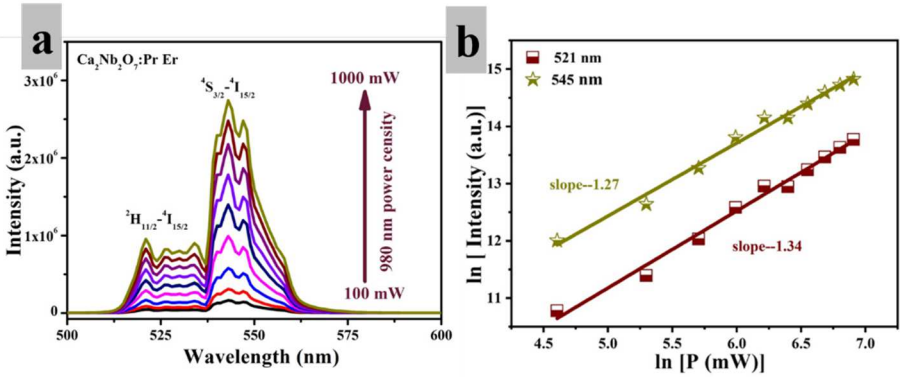

Fig. 5. (a) The upconversion emission spectra of the $Ca_2Nb_2O_7$:Pr/Er sample with different pumping powers under 980 nm excitation. (b) The upconversion emission intensity at 521 and 545 nm versus pumping powers for the $Ca_2Nb_2O_7$:Pr/Er sample.

In addition to the above-mentioned conversion of down-shifting UV excitation to

visible emission, Er^{3+} ions are considered as effective ions for upconversion emission, which can be generally excited by near-infrared light[38]. Thus, the upconversion emission spectra has been recorded under 980 nm excitation. Under the excitation by 980 nm, all luminescence centers come from Er^{3+} ions, independent of Pr^{3+} ions. Among them, the emission spectra consisting of strong green emission bands at 521 and 545 nm originate from the transition from $^2H_{11/2}$ to $^4I_{15/2}$ and $^4S_{3/2}$ to $^4I_{15/2}$ of Er^{3+} ions, respectively[39]. The peak position doesn't change on account of the energy level transition of Er^{3+} with the different power intensity from 100 mW to 1000 mW. Our findings indicate that color from the weaker green changes to the stronger green with the gradually power intensity increasing. To further analyze the upconversion luminescence mechanisms, the luminescence intensity at 521 and 545 nm was studied with different pump power. The intensity of upconversion emission (I_{UC}) and the excitation power (P) can be expressed as follows: $I_{UC} \propto P^n$,, the index n is the number of photons absorbed by the luminescent centers. As indicated in Fig. 4b, the linear fitting slopes of samples are 1.34 and 1.27, corresponding to the upconversion emission intensity versus pumping power at 521 and 545 nm, respectively. It indicates that the transition of Er^{3+} ions in the $Ca_2Nb_2O_7$ matrix is a two-photon upconversion process.

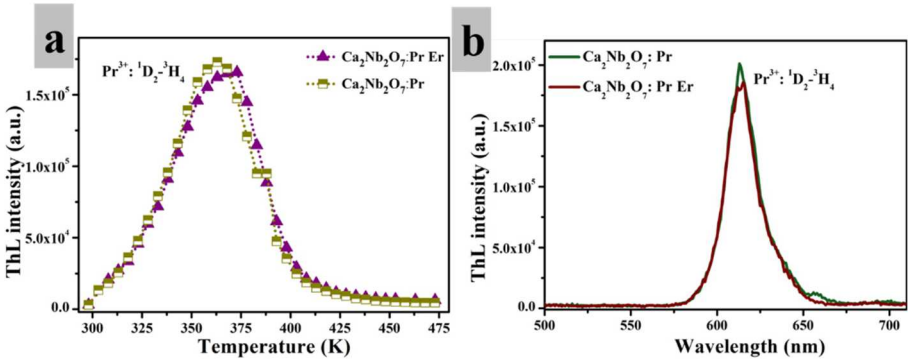

Fig. 6. (a) The thermoluminescence (ThL) curves of Pr^{3+}-doped and Pr^{3+}/Er^{3+} codoped samples, respectively. (b) The ThL emission spectra of Pr^{3+}-doped and Pr^{3+}/Er^{3+} codoped samples at 360 K.

The thermal stimulated luminescence is an interesting phenomenon for luminescent materials[40, 41]. In order to clarify the depth and density of the traps, Fig. 6a shows the ThL curves of Pr^{3+}-doped and Pr^{3+}/Er^{3+} codoped samples. At first, the prepared sample was exposed under a UV lamp irradiation (365 nm) for 1 min at room temperature. Then a red persistent luminescence can be observed by naked eye for almost 30 s. After two minutes, we heated up the sample and recorded its luminous intensity as the temperature changes finally. When it was heated to around 360 K, a beam of red light can be observed and the luminous intensity reached the maximum. What is more, when the sample was heated to higher temperature, the luminous intensity decreased. Our results show that the incorporated Pr^{3+} ions acted as new trapping levels within the system, which resulted in the red long-persistent luminescence. Among them, the Pr^{3+} dopants in $Ca_2Nb_2O_7$ act the dual role as fluorescent centers and trapping centers, while the Er^{3+} dopants act as fluorescent centers only. Besides, we have also observed that there is no thermoluminescence in the $Ca_2Nb_2O_7:Er^{3+}$ sample and this result is consistent with previous reports[28]. The

thermally released hole or electron recombines with the opposite charge at Pr^{3+} level and this electron–hole recombination results in the emission of visible light. Due to the difference of the electronic structure of Pr^{3+} and Er^{3+}, Er^{3+} doesn't form traps at suitable level so that the charge trapping is not possible. The ThL curves and peak position are two important parameters for analyzing traps, the former reflects the density of the trap, and the latter reflects the depth of the trap[42]. Compared with the sample single-doped with Pr^{3+}, the intensity of the ThL curve in the Pr^{3+}/Er^{3+} codoped sample is not much different. The position of temperature corresponding to the highest luminous intensity in the curve slightly shifts to high temperature, indicating the trap depth becomes deeper with the doping of Er^{3+}. According to the previous literature reports, the trap energy level corresponding to the thermal release peak can be approximated by the following relationship: $E=T_m/500$, where E is the trap depth, and T_m corresponds to the thermal release peak position temperature[43]. Therefore, the trap depths in $Ca_2Nb_2O_7:Pr^{3+}$ and $Ca_2Nb_2O_7:Pr^{3+}/Er^{3+}$ can be calculated as 0.726 eV and 0.746 eV, respectively. The lower trap density in $Ca_2Nb_2O_7:Pr^{3+}$ compared with $Ca_2Nb_2O_7:Pr^{3+}/Er^{3+}$ may due to the smaller ionic size of Er^{3+} (0.881 Å) than that of Pr^{3+} (0.101 Å), which results in more non-radiative lattice defects.

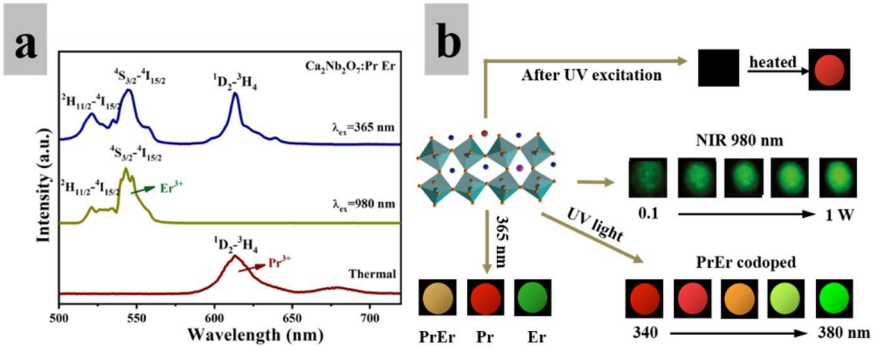

Fig. 7. (a) The emission spectra of the $Ca_2Nb_2O_7:Pr^{3+}/Er^{3+}$ sample under different

excitation modes, including UV light at 365 nm, 980 nm NIR laser and thermal stimuli. (b) The schematic diagram of multi-mode responsive emissions for multi-dimensional anticounterfeiting.

In order to prove that the $Ca_2Nb_2O_7$ system material doped with lanthanide ions has multifunctional fluorescence characteristic. We recorded their different luminescence responses in different modes, as shown in the Fig. 7. It can be seen from Fig. 7a that the $Ca_2Nb_2O_7:Pr^{3+}/Er^{3+}$ sample can generate different emission spectra under different excitation modes, including UV light at 365 nm, 980 nm NIR laser and thermal stimuli. In our work, the developed samples include $Ca_2Nb_2O_7:Pr^{3+}$, $Ca_2Nb_2O_7:Er^{3+}$ and $Ca_2Nb_2O_7:Pr^{3+}/Er^{3+}$. Fig. 7b displays the developed samples under different stimuli. Under 365 nm excitation, $Ca_2Nb_2O_7:Pr^{3+}/Er^{3+}$ showed brown color, $Ca_2Nb_2O_7:Pr^{3+}$ presented red, while $Ca_2Nb_2O_7:Er^{3+}$ displayed green. For the $Ca_2Nb_2O_7:Pr^{3+}/Er^{3+}$ sample, its fluorescence color changed from red to orange to green as well as excitation wavelengths increased from 340 to 380 nm. While under 980 nm excitation, changing the excitation power of the laser from 100 mW to 1000 mW, the color of $Ca_2Nb_2O_7:Er^{3+}$ and $Ca_2Nb_2O_7:Pr^{3+}/Er^{3+}$ samples changed from a weaker green to a brighter green. The $Ca_2Nb_2O_7:Pr^{3+}$ and $Ca_2Nb_2O_7:Pr^{3+}/Er^{3+}$ samples have ThL properties. After irradiating under 365 nm lamp for 1 min, and then waited for 2 min, the sample could not be observed emission. Interestingly, when the sample was heated to 373 K, and it would generate red emission. All the above experiments have a good repeatability and stability. Because of its excellent multi-mode luminescence performance, it can be applied in the field of optical anti-counterfeiting.

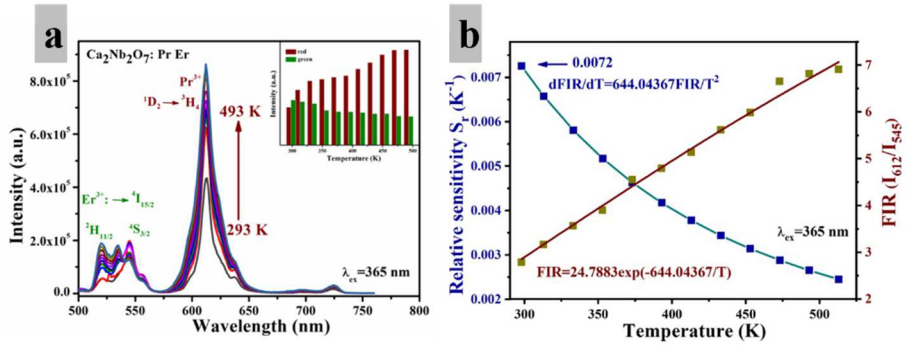

Fig. 8. (a) The temperature dependent emission spectra between 500 and 700 nm under 365 nm excitation. The inset indicates the change law of luminous intensity with different temperature located at 545 and 612 nm regions. (b) The fluorescence intensity ratio (FIR) versus temperature within the range from 293 to 493 K and Relative sensitivity (S_r) versus temperature.

So far, the optical temperature sensing based on FIR has mainly focused on lanthanide doped upconversion materials[44]. For example, the results of Diaz's group showed that YVO_4:Yb^{3+}/Er^{3+} and $GdVO_4$:Yb^{3+}/Er^{3+} nanoparticles have a good temperature sensing property and achieved enhancement of the sensitivity using a SiO_2 coating[45]; Sun's group showed that YF_3:Er^{3+}/Yb^{3+} nanocrystals are ideal upconversion materials for optical temperature sensors based on FIR and they proved that the sensitivity of their materials increases with the decrease of the particle size[46]. However, in the above works, the efficiency of upconversion emission excited by 980nm laser or other near-infrared light sources is relatively low. It's noted that the UV lights are widely used because of its low cost and convenience. That is why we choose the most common 365 nm UV light to discuss the temperature characteristics of the codoped sample. Fig. 8a shows the emission spectra of $Ca_2Nb_2O_7$:Pr^{3+}/Er^{3+} sample under the excitation of 365 nm in the temperature range from 293 to 493 K. As the temperature increases, the intensity of the two emitted thermally coupled energy levels changes corresponding to Pr^{3+} and Er^{3+} ions,

respectively. It can be found from the obtained spectrum that their spectra maintain the same shape except for intensity when the temperature increases. The positions of neither the green nor the red emission peak shift, but the intensity varies significantly. Furthermore, the intensity of emission peaks locates at 610 and 521 nm increases with rising temperature. By contrast, the intensity of emission peaks located at 545 nm decreases with rising temperature (inset of Fig. 8a). Therefore, a different behavior was observed of the prepared sample is that the intensity of the emission peak varies with temperature. This temperature-dependent behavior of emission intensity can be described by the FIR of the two peaks at 612 and 545 nm, which is a great signal recognition ability in detecting temperature. The FIR corresponding to the two thermal coupling levels follows the formula[47]:

$$\mathrm{FIR} = \frac{I_2}{I_1} = \frac{g_2\sigma_2\omega_2}{g_1\sigma_1\omega_1}\exp\left[-\frac{\Delta E}{kT}\right] = Bexp[-\frac{\Delta E}{kT}]. \quad (1)$$

Wherein, I_2 and I_1 denote the emission intensity of two emission peaks, g_i represents the degenerate energy level, T represents the absolute temperature, B and k_b are constants, and ΔE is the energy gap between two energy levels. In the temperature range from 293 to 493 K, the scatter diagram of I_{612}/I_{545} with temperature changes is shown as the yellow dot in Fig. 8b. In this temperature range, I_{612}/I_{545} has a great exponential relationship with temperature T, which can be expressed by formula: FIR=24.7883exp(-644.04367/T). In order to understand the temperature measurement capability of the material deeply, its sensitivity was analyzed. The results are shown in Fig. 8b. It can be seen from the figure that blue line indicates the S_r, which characterizes the sensitivity of the fluorescence intensity to temperature. In this part, the S_r as an important parameter can be calculated as: S_r=dFIR/dT=FIR(-ΔE/kT)[48].

For the study of temperature sensing characteristics, the value of S_r is more important than the absolute sensitivity[49]. Therefore, it can be seen from the figure that in the

temperature range from 293 to 493 K, the maximum temperature sensitivity is 0.0072 K^{-1} at 293 K.

4. Conclusions

In summary, we have developed a kind of multi-mode luminescent material, lanthanide-doped piezoelectric calcium niobates, for anti-counterfeiting and temperature sensing. Under 365 nm excitation, the compounds could be observed brown, red and blue emissions corresponding to $Ca_2Nb_2O_7:Pr^{3+}/Er^{3+}$, $Ca_2Nb_2O_7:Pr^{3+}$ and $Ca_2Nb_2O_7:Er^{3+}$, respectively. For the $Ca_2Nb_2O_7:Pr^{3+}/Er^{3+}$ sample, the luminescence emission color is adjustable from red to orange to green when the excitation wavelength increases from 340 to 380 nm. For upconversion luminescence, changing the laser power could change the color of the sample from weak green to stronger green. Moreover, the prepared samples also generate emissions under thermal stimuli. The prepared materials not only have excellent performance in multi-mode luminescence, but also can be used for temperature sensing. The temperature sensor is constructed on the thermal coupling energy levels of Pr and Er ions under the excitation of 365 nm. The optical temperature sensitivity could be up to 0.0072 K^{-1}. These results suggest that prepared luminescent materials have great potential applications in the field of multi-functional device, optical anti-counterfeiting and temperature sensing.

CRediT author statement

Wen Yan: Writing - original draft, Data curation, Writing - review & editing.

Zewen Su: Writing - review & editing.

Renguang Ye*: Methodology.

Liang Chen: Methodology, Resources.

Zhanling Lu: Methodology.

Gongxun Bai*: Conceptualization, Supervision, Writing - review & editing.

Shiqing Xu*: Conceptualization, Supervision.

Acknowledgments

This work was supported by Zhejiang Provincial Natural Science Foundation of China (No LZ21E020004, LD18F050001), Chinese National Natural Science Foundation (No U1909211, 61705214), the Fundamental Research Funds for the Provincial Universities of Zhejiang and Science and Technology Innovation Platformand Talent Plan of Zhejiang.

Conflict of Interest

There are no conflicts to declare.

References

[1] H. Kang, J. Lee, Y. Nam, Inkjet-printed multiwavelength thermoplasmonic images for anticounterfeiting applications, ACS Appl. Mater. Inter. 10 (2018) 6764-6771.

[2] Y. Meng, F. Liu, M. Umair, B. Ju, S. Zhang, B. Tang, Patterned and iridescent plastics with 3D inverse opal structure for anticounterfeiting of the banknotes, Adv. Opt. Mater. 6 (2018) 1701351.

[3] V. Singh, R. Chitumalla, S. Ravi, Y. Zhang, Y. Xi, V. Sanjairaj, C. Zhang, J. Jang, S. Tan, Inkjet-printable hydrochromic paper for encrypting information and anticounterfeiting, ACS Appl. Mater. Inter. 9 (2017) 33071-33079.

[4] W. Park, T. Ha, T.S. Jung, K.I. Sim, J.H. Kim, et al., Security use of the chiral photonic film made of helical liquid crystal structures, Nanoscale 12 (2020) 21629-21634.

[5] W. Hu, T. Li, X. Liu, D. Dastan, K. Ji, P. Zhao, 1550 nm pumped upconversion chromaticity modulation in Er^{3+} doped double perovskite $LiYMgWO_6$ for anti-counterfeiting, J. Alloys Compd. 818 (2020) 152933.

[6] P. Martinez, I. Papagiannouli, D. Descamps, et al., Laser generation of sub-micrometer wrinkles in a chalcogenide glass film as physical unclonable functions, Adv. Mater. 32 (2020) 2003032.

[7] C. Zhang, X. Li, M. Liu, T. Li, et al., Dual-wavelength stimuli and green emission response in lanthanide doped nanoparticles for anti-counterfeiting, J. Alloys Compd. 836 (2020) 155487.

[8] Y. Wang, X. Tian, H. Zhang, Z. Yang, X. Yin, Anticounterfeiting quick response code with emission color of invisible metal-organic frameworks as encoding information, ACS Appl. Mater. Inter. 10 (2018) 22445-22452.

[9] D. Wales, Q. Cao, K. Kastner, E. Karjalainen, G.N. Newton, V. Sans, 3D-printable photochromic molecular materials for reversible information storage, Adv. Mater. 30 (2018) 1800159.

[10] C. Peng, C. Hsu, C. Li, P. Wang, C. Jeng, C. Chang, G. Wang, Flexible photonic crystal material for multiple anticounterfeiting applications, ACS Appl. Mater. Inter. 10 (2018) 9858-9864.

[11] R. Yang, Y. Zhu, F. Chen, L. Dong, Z. Xiong, Luminescent, fire-resistant, and water-proof ultralong hydroxyapatite nanowire-based paper for multimode anticounterfeiting applications, ACS Appl. Mater. Inter. 9 (2017) 25455-25464.

[12] X. Liu, Y. Wang, X. Li, Z. Yi, R. Deng, L. Liang, X. Liu, et al., Binary temporal upconversion codes of Mn^{2+}-activated nanoparticles for multilevel anti-counterfeiting, Nat. Commun. 8 (2017) 899.

[13] Z. Kennedy, D. Stephenson, J. Christ, T. Pope, B. Arey, C. Barrett, M. Warner, Enhanced anti-counterfeiting measures for additive manufacturing: coupling lanthanide nanomaterial chemical signatures with blockchain technology, J. Mater. Chem. C 5 (2017) 9570-9578.

[14] S. Wang, J. Lin, Y. He, J. Chen, D. Chen, Remarkable laser-driven upconverting photothermal effect of Cs_3LnF_6@glass nanocomposites for anti-counterfeiting, Chem. Eng. J. 394 (2020) 124889.

[15] J. Lin, C. Yang, P. Huang, S. Wang, M. Liu, N. Jiang, D. Chen, Photoluminescence tuning from glass-stabilized $CsPbX_3$ (X = Cl, Br, I) perovskite nanocrystals triggered by upconverting Tm: KYb_2F_7 nanoparticles for high-level anti-counterfeiting, Chem. Eng. J. 395 (2020) 125214.

[16] D. Tu, C. Xu, A. Yoshida, M. Fujihala, J. Hirotsu, X. Zheng, $LiNbO_3$: Pr^{3+}: A multipiezo material with simultaneous piezoelectricity and sensitive piezoluminescence, Adv. Mater. 29 (2017) 1606914.

[17] N. Syed, A. Zavabeti, J. Ou, M. Mohiuddin, B. Zhang, et al., Printing two-dimensional gallium phosphate out of liquid metal, Nat. Commun. 9 (2018) 3618.

[18] Y. Zhong, B. Deng, X. Gao, P. Sun, Y. Ren, T. Liang, R. Yu, High thermally Sm^{3+}-activated $SrBi_2Ta_2O_9$ orange-red phosphor: preparation, characterization, and optical properties, J. Lumin. 215 (2019) 116648.

[19] J. Wu, N. Qin, E. Lin, B. Yuan, Z. Kang, D. Bao, Synthesis of $Bi_4Ti_3O_{12}$ decussated nanoplates with enhanced piezocatalytic activity, Nanoscale 11 (2019) 21128-21136.

[20] Z. Gao, H. Ning, C. Chen, R. Wilson, B. Shi, H. Ye, H. Yan, M. Reece, The effect of barium substitution on the ferroelectric properties of $Sr_2Nb_2O_7$ ceramics, J. Am. Ceram. Soc. 96 (2013) 1163-1170.

[21] J. Zhang, Y. Liu, X. Yan, H. Zhang, J. Zhang, X. Wang, W. Han, et al., Multicolor tuning in room-temperature self-activated $Ca_2Nb_2O_7$ submicroplates by lanthanide doping, Chemphyschem 18 (2017) 269-273.

[22] G. Bai, M. Tsang, J. Hao, Luminescent ions in advanced composite materials for multifunctional applications, Adv. Funct. Mater. 26 (2016) 6330-6350.

[23] Y. Huang, L. Luo, W. Cheng, The color-tunable up-conversion photoluminescence properties of $Na_{0.5}Bi_{0.5}TiO_3:Yb^{3+}/Tm^{3+}$ ceramics and its temperature sensing application based on the intrinsic defects, J. Alloys Compd. 797 (2019) 659-665.

[24] R. Basavaraj, H. Nagabhushana, G. Darshan, B. Prasad, et al., Red and green emitting CTAB assisted $CdSiO_3:Tb^{3+}/Eu^{3+}$ nanopowders as fluorescent labeling agents used in forensic and display applications, Dyes Pigm. 147 (2017) 364-377.

[25] F. Kang, G. Sun, A. Wang, X. Xiao, Y. Li, J. Lu, B. Huang, Multicolor tuning and temperature-triggered anomalous Eu^{3+}-related photoemission enhancement via interplay of accelerated energy transfer and release of defect-trapped electrons in the Tb^{3+}, Eu^{3+} doped strontium-aluminum chlorites, ACS Appl. Mater. Inter. 10 (2018) 36157-36170.

[26] H. Huang, J. Chen, Y. Liu, J. Lin, S. Wang, F. Huang, D. Chen, Lanthanide-doped core@multishell nanoarchitectures: multimodal excitable upconverting/downshifting luminescence and high-level anti-counterfeiting, Small 16 (2020) 2000708.

[27] S. Xie, G. Gong, Y. Song, H. Tan, C. Zhang, et al., Design of novel lanthanide-doped core-shell nanocrystals with dual up-conversion and down-conversion luminescence for anti-counterfeiting printing, Dalton Trans. 48 (2019) 6971-6983.

[28] J. Zhang, C. Pan, Y. Zhu, L. Zhao, H. He, X. Liu, J. Qiu, Achieving thermo-mechano-opto-responsive bitemporal colorful luminescence via multiplexing of dual lanthanides in piezoelectric particles and its multidimensional anticounterfeiting, Adv. Mater. 30 (2018) 1804644.

[29] C. Shi, X. Shen, Y. Zhu, X. Li, Z. Pang, M. Ge, Excitation wavelength-dependent dual-mode luminescence emission for dynamic multicolor anticounterfeiting, ACS Appl. Mater. Inter. 11 (2019) 18548-18554.

[30] Y. Tomashpolsky, V. Matyuk, N. Sadovskaya, Mechanisms of the formation of a surface phase with the matrix composition in a $Ca_2Nb_2O_7$ single crystal, Inorg. Mater. 52 (2016) 791-795.

[31] D. Yang, P.a. Ma, Z. Hou, Z. Cheng, C. Li, J. Lin, Current advances in lanthanide ion (Ln^{3+})-based upconversion nanomaterials for drug delivery, Chem. Soc. Rev. 44 (2015) 1416-1448.

[32] C. Wu, Y. Li, H. Gong, J. Gao, Z. Wang, Niobium-oxygen octahedra and oxygen interstitial defect emissions in calcium niobate matrix and its color manipulation via doping Pr^{3+}, AIP Adv. 7 (2017) 025019.

[33] H. Sun, X. Li, Y. Zhu, X. Wang, Q. Zhang, X. Hao, Achieving multicolor emission readout and tunable photoswitching via multiplexing of dual lanthanides in ferroelectric oxides, J. Mater. Chem. C 7 (2019) 5782-5791.

[34] M. Tsang, G. Bai, J. Hao, Stimuli responsive upconversion luminescence nanomaterials and films for various applications, Chem. Soc. Rev. 44 (2015) 1585-1607.

[35] X. Wu, T. Chung, H. Sun, K. Kwok, Tunable photoluminescence properties of Pr^{3+}/Er^{3+}-doped $0.93Bi_{0.5}Na_{0.5}TiO_3$-$0.07BaTiO_3$ low-temperature sintered multifunctional ceramics, Ceram. Int. 42 (2016) 9899-9905.

[36] F. Hu, J. Cao, X. Wei, X. Li, J. Cai, H. Guo, Y. Chen, C. Duan, M. Yin, Luminescence properties of Er^{3+}-doped transparent $NaYb_2F_7$ glass-ceramics for optical thermometry and spectral conversion, J. Mater. Chem. C 4 (2016) 9976-9985.

[37] Y. Tian, Y. Tian, P. Huang, L. Wang, Q. Shi, C.e. Cui, Effect of Yb^{3+} concentration on upconversion luminescence and temperature sensing behavior in Yb^{3+}/Er^{3+} co-doped $YNbO_4$ nanoparticles prepared via molten salt route, Chem. Eng. J. 297 (2016) 26-34.

[38] P. Liu, J. Liu, Y. Zhang, Z. Xia, Y. Xu, Morphology controlled synthesis of $Ba_4Bi_3F_{17}:Er^{3+}$, Yb^{3+} and the dual-functional temperature sensing and optical heating applications, J. Alloys Compd. 844 (2020) 156116.

[39] H. Sun, Q. Zhang, X. Wang, M. Gu, Green and red upconversion luminescence of Er^{3+}-doped $K_{0.5}Na_{0.5}NbO_3$ ceramics, Ceram. Int. 40 (2014) 2581-2584.

[40] Y. Tao, R. Chen, H. Li, J. Yuan, Y. Wan, H. Jiang, C. Chen, et al., Resonance-activated spin-flipping for efficient organic ultralong room-temperature phosphorescence, Adv. Mater. 30 (2018) 1803856.

[41] C. Pedroso, J. Carvalho, L. Rodrigues, J. Holsa, H. Brito, Rapid and energy-saving microwave-assisted solid-state synthesis of Pr^{3+}, Eu^{3+}, or Tb^{3+}-doped Lu_2O_3 persistent luminescence materials, ACS Appl. Mater. Inter. 8 (2016) 19593-19604.

[42] A. Abdukayum, J. Chen, Q. Zhao, X. Yan, Functional near infrared-emitting Cr^{3+}/Pr^{3+} Co-Doped Zinc gallogermanate persistent luminescent nanoparticles with superlong afterglow for in vivo targeted bioimaging, J. Am. Chem. Soc. 135 (2013) 14125-14133.

[43] T. Katsumata, S. Toyomane, A. Tonegawa, Characterization of trap levels in long-duration phosphor crystals, J. Cryst. Growth. 237 (2002) 361-366.

[44] P. Du, J. Yu, Near-ultraviolet light induced visible emissions in Er^{3+}-activated La_2MoO_6 nanoparticles for solid-state lighting and non-contact thermometry, Chem. Eng. J. 327 (2017) 109-119.

[45] O. Savchuk, J. Carvajal, C. Cascales, M. Aguilo, F. Diaz, Benefits of silica core-shell structures on the temperature sensing properties of Er,Yb:$GdVO_4$ up-conversion nanoparticles, ACS Appl. Mater. Inter. 8 (2016) 7266-7273.

[46] Q. Meng, T. Liu, J. Dai, W. Sun, Study on optical temperature sensing properties of YVO_4:Er^{3+}, Yb^{3+} nanocrystals, J. Lumines. 179 (2016) 633-638.

[47] L. Marciniak, A. Pilch, S. Arabasz, D. Jin, A. Bednarkiewicz, Heterogeneously Nd^{3+} doped single nanoparticles for NIR-induced heat conversion, luminescence, and thermometry, Nanoscale 9 (2017) 8288-8297.

[48] J. Zhong, D. Chen, Y. Peng, Y. Lu, X. Chen, X. Li, Z. Ji, A review on nanostructured glass ceramics for promising application in optical thermometry, J. Alloys Compd. 763 (2018) 34-48.

[49] H. Suo, X. Zhao, Z. Zhang, T. Li, E. Goldys, C. Guo, Constructing multiform morphologies of YF: Er^{3+}/Yb^{3+} up-conversion nano/micro-crystals towards sub-tissue thermometry, Chem. Eng. J. 313 (2017) 65-73.